



## Research article

Plasticized magnetic starch-based Fe<sub>3</sub>O<sub>4</sub> clay polymer nanocomposites for phosphate adsorption from aqueous solutionTesfalem Atnafu<sup>a,b,\*</sup>, Seyoum Leta<sup>a</sup><sup>a</sup> Center for Environmental Science, Addis Ababa University, P.O.Box 1176, Addis Ababa, Ethiopia<sup>b</sup> Department of Biological Science, Mettu University, P.O.Box 318, Mettu, Ethiopia

## ARTICLE INFO

## Keywords:

Phosphate adsorption  
 Polymer nanocomposite (PNC)  
 Magnetic nanoparticles  
 Activated carbon (AC)  
 Starch

## ABSTRACT

Plastics contribute a magnificent role to modern civilization, but the waste becomes a huge burden to ecology and remains intact for a thousand years. Hence, the recent movement is shifted to biodegradable plastic. In this study, an attempt was made to introduce an added value to the environment where the bio-plasticized materials were used for phosphate removal. A G-plasticized magnetic starch-based Fe<sub>3</sub>O<sub>4</sub> clay polymer nanocomposite (PNC) was synthesized to remove phosphate from the aqueous solution. It was synthesized from activated carbon (AC), coated iron oxide nanoparticles (CIONP), nanoclay (NC), and glycerol (G) as a plasticizer. The synthesized adsorbents were characterized with UV-Vis, SEM, XRD, and FTIR. The PNC and constituent (CIONP) were tested for phosphate removal through batch adsorption experiments. The adsorption capacity increases with increasing the adsorbent dose and decreases with an increase in phosphate concentration. The synthesized PNC effectively raised the constituent optimum phosphate ion adsorption pH from acidic (pH = 3) to slightly acidic (pH = 6). At the optimal pH, the CIONP and PNC maximum phosphate adsorption capacity (MPAC) was 3.12 and 2.31 mg P/g, respectively. In addition, the phosphate removal efficiency of PNC (45-95% at pH 6) was comparable to CIONP (58-97% at pH 3) under an initial 2–100 mg P/L. The adsorbents adsorption kinetics and isotherm study best described by the pseudo-second-order and Freundlich model, in turn. The SEM images support the conclusion, in which the PNC shows a heterogenous porous surface. Therefore, the adsorption mechanisms were mainly described by multilayer and chemical adsorption, such as electrostatic and ion exchange. It can be concluded that there is a positive synergistic effect between the biopolymer (starch) and nanomaterials that form the PNC. This study results propose the multiple added values of modified bio-plasticized material (with adsorbent) for environmental (phosphate) remediation.

## 1. Introduction

Plastics production increases globally, since its discovery in 1907, especially from 1950 (2 million tons) to 2015 (8.3 billion tons) (Moharir & Kumar, 2019), and accounts for trillions of dollars of the global economy (Reddy et al., 2013). However, the plastics lifespan, mainly single-use plastic bags, are on average 12–15 min but remain 10–1000 years in the environment (UNDP, 2021) or reside in the environment several times away from the production target use. Worldwide 50 kg/year/capita plastic waste is produced, and 8 million tons/year is dumped into the ocean (Mazhandu et al., 2020). Plastic pollution is a critical concern due to being non-biodegradable and causes health hazard problems.

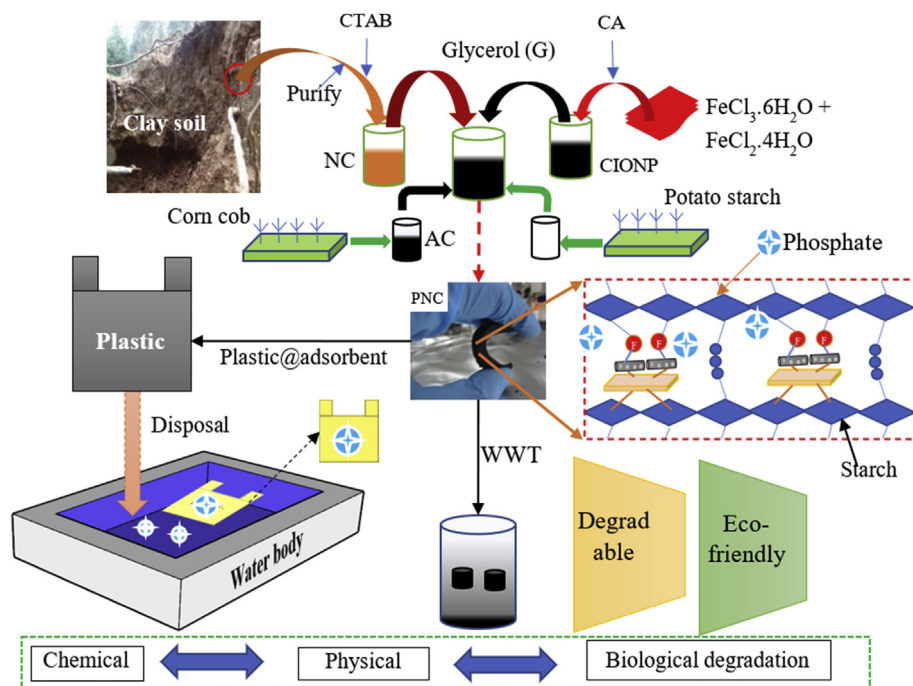
So far, different alternatives were proposed to reduce plastic pollution such as producing biodegradable plastics, recycling, reuse, convert into value-added products, or eco-friendly disposal. According to the United States Environmental Protection Agency, in 2003, about 236 million tons of municipal waste generated from this 11.3% was plastic, and only a small fraction was recovered, but the major portion was disposed (Zheng et al., 2005). An eco-friendly technique to dispose of plastic through application in construction or flexible pavements was reported by Vasudevan et al. (2012). Plastic life cycle assessment study by Al-Salem et al. (2014) indicates the problems with the existing alternative technologies for plastic waste management such as thermo-chemical treatment to convert plastics into waxes, naphtha, syncrude, and e-gas (comparable to natural gas). Besides the financial issue, the process

\* Corresponding author.

E-mail address: [tesfalem\\_atnafu@yahoo.com](mailto:tesfalem_atnafu@yahoo.com) (T. Atnafu).<https://doi.org/10.1016/j.heliyon.2021.e07973>

Received 6 July 2021; Received in revised form 23 August 2021; Accepted 7 September 2021

2405-8440/© 2021 The Author(s). Published by Elsevier Ltd. This is an open access article under the CC BY-NC-ND license (<http://creativecommons.org/licenses/by-nc-nd/4.0/>).



**Scheme 1.** Schematic representation of G-plasticized magnetic starch-based  $\text{Fe}_3\text{O}_4$  clay polymer nanocomposite preparation and phosphate removal. where P = phosphorus and WWT = Wastewater treatment. For details see Scheme 2 (supporting information).

**Table 1.** Physicochemical properties of raw clay soil.

Parameters	Raw clay	
	Black clay	Red clay
pH (-)	5.24	5.89
EC (mS/cm)	0.37	0.04
Sand (%)	57.00	3.00
Clay (%)	37.00	85.00
Silt (%)	6.00	12.00
$\text{CaCO}_3$ (%)	3.35	4.38
Organic carbon (%)	5.46	0.08
Organic matter (%)	9.41	0.14
TN (%)	0.41	0.01
CEC (meq/100 g soil)	52.86	30.53
C: N	13.41	8.00
Bulk density (BD) ( $\text{g}/\text{cm}^3$ )	1.18	1.11
Texture class	Sandy Clay	Heavy Clay

releases greenhouse gas emissions (hydrocracking) and eutrophication (pyrolysis).

Hence, the recent view is toward biodegradable and eco-friendly plastics from biopolymers produced by certain living organisms (Moharir & Kumar, 2019). The biodegradable plastics concept focuses on (1) blending the traditional polyethylene (PE) with degradable materials (e.g., starch), (2) biodegradable polyesters include polylactic acid and thermoplastic starch-based polymers, and (3) aliphatic co-polyesters such as polyhydroxyalkanoates (PHAs) produced by bacteria as energy storage means (Reddy et al., 2013). The renewable, biodegradable plastics are from potato, corn, or wheat starch-based plastics (Zheng et al., 2005). However, the production process and cost are still the bottlenecks (Kumar et al., 2020; Mazhandu et al., 2020). In turn, the plastics additives (blend) results in a chain of harmful effects on the environment; in addition, when the plastics materials degrade releases micro- or nano-plastics (size  $<5$  mm/ $<100$  nm), which are an emerging threat to the environment (Kumar et al., 2021).

Therefore, to address the plastics challenge may demand a novel concept. Anti-bacterial doped plasticized materials demand for food packaging is escalating to increase food shelf-life (Syafiq et al., 2021). Building on this notion, developing a biodegradable plastic material that is again used as a pollution remedy seems sustainable plastic from an environmental point of view. Plasticized materials could be doped with adsorbents to remove phosphorus (P), heavy metals, and even salts from the aquatic environment. Therefore, when the plastic materials are dumped into the environment, they could act as a versatile material that removes pollutants and contributes to the degradation rate.

Among the pollutants, P is the major nutrient for sustaining life on earth (Waweru et al., 2019) and the normal functioning of the ecosystem (Liu and Zhang, 2015). However, excess phosphate concentration of P as 0.02–0.39 mg P/L causes eutrophication, pollutes the water bodies, and 0.75–1.20 mg P/L is called hypereutrophic (De Castro et al., 2019; Yang et al., 2019). As a result, in most countries, recommended effluent phosphate concentrations were generally  $<2$  mg P/L despite variation based on the receiving water bodies sensitivity: for example, European Union, directive 91/271/EE endorses 1–2 mg P/L of total phosphorus (TP) in the discharge effluent (Peleka and Deliyanni, 2009).

In cells, phosphorus is found as ATP (adenosine triphosphate) and DNA/RNA (deoxyribonucleic acid/ribonucleic acid), whereas in water available as particulate and dissolved phosphate: organic or inorganic (orthophosphate or soluble reactive) (De Castro et al., 2019). So far, several technologies have been developed to remove P. Relative to available technologies, adsorption is considered an effective P removal method due to its simplicity in operation and economical (Peleka and Deliyanni, 2009), fast and high removal efficiency at trace level (Huang et al., 2017), and produce less amount of sludge (Jiang et al., 2013).

The maximum phosphate uptake by various adsorbents was at an acidic pH ( $\leq 5.0$ ) (Dai et al., 2011) or basic pH (Santos et al., 2019). Often, the adsorbents optimum phosphate ion adsorption pH is far from near-neutral and mostly favor acidic; for example, activated carbon (AC) at pH 4 (3.2 mg P/g), fly ash at pH 11–12 (30–36 mg P/g), magnetic iron-oxide nanoparticles (IONPs) at pH 2.0 (5.03 mg P/g) (Yoon et al., 2014), alum sludge at pH 4 (32 mg P/g), and calcined eggshell at pH 8.0 (96.1%) (Santos et al., 2019). However (Nakarmi et al., 2020), observed

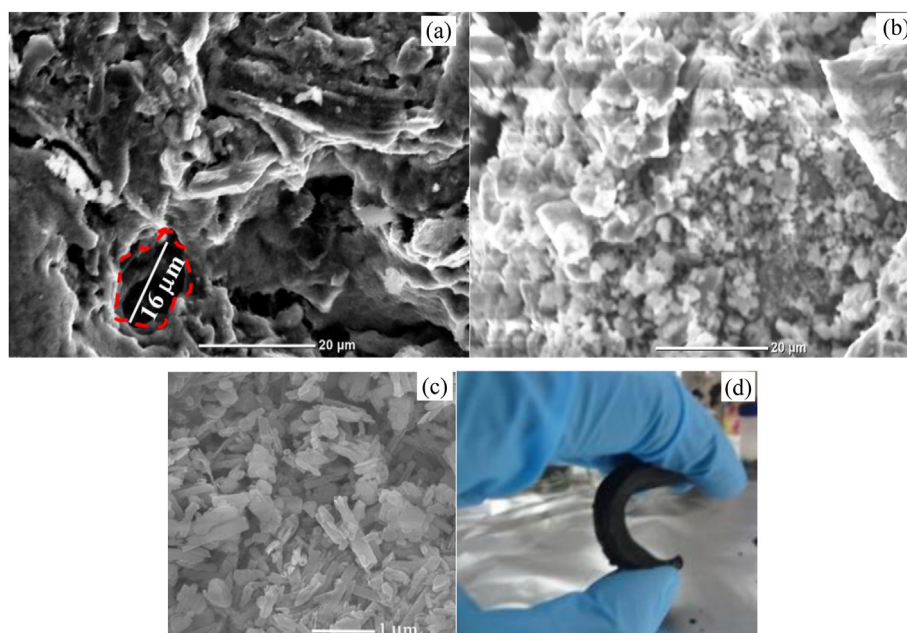


Figure 1. SEM images of C9ST (a) before and (b) after phosphate adsorption, (c) activated carbon, and (d) photo of C9ST.

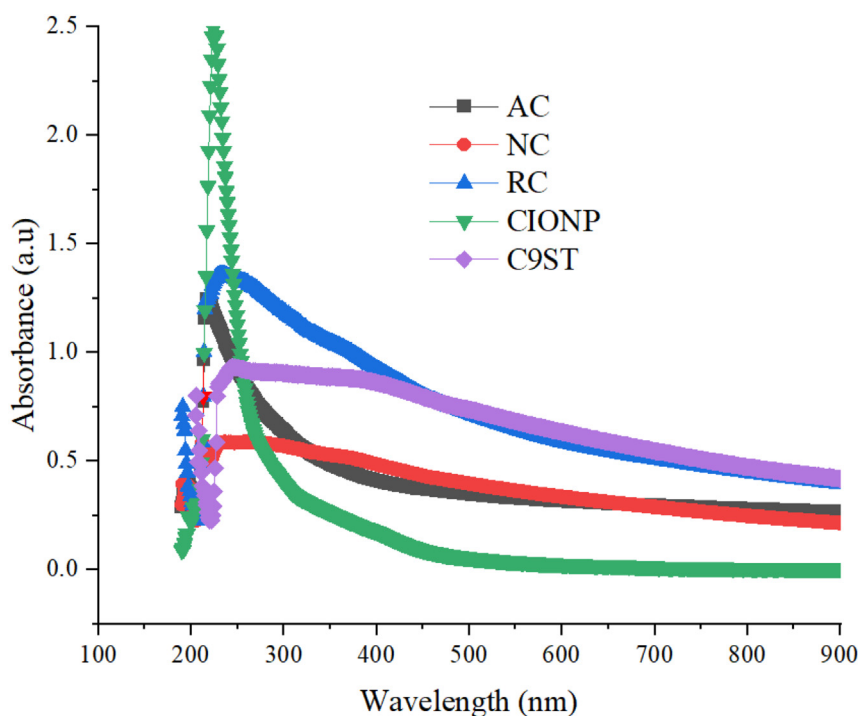


Figure 2. UV-Vis analysis of constituents and G-plasticized magnetic starch clay polymer nanocomposite (C9ST).

maximum phosphate uptake (265.5 mg P/g) using zinc oxide betaine modified biochar nanocomposites (ZnOBBNC) at pH 7, but a day-long extended contact time (24 h). Yang et al. (2019) noted superior P adsorption capacity (152.1 mg P/g) of B-Zn/Al-LDH composite at pH 5.

Nanoparticles are becoming the most widely used in wastewater treatment (Padmavathy et al., 2016). IONPs ( $\text{Fe}_3\text{O}_4$ ) were studied very well because of their super magnetic, catalytic, high surface-to-volume ratio (SVR), and unique electronic properties (Ali et al., 2017; Juang et al., 2018). Additionally, phosphate ion adsorption by iron is significantly affected by increasing the pH from 3 (96.4%) to 4.5 (48.4%), and the further increase critically lowers the capacity (Nagoya et al., 2019).

However, clay is a well-known natural hydrophilic adsorbent but has a limited application for cationic pollutants in pure form. Clay modification is essential in such conditions through organic or inorganic cations, magnetic particles, or pillaring using metals or converting them into nanoclay (NC). AC can remove wide organic molecules, but less removal efficiency was reported for organic or hydrophilic compounds like humic acid, emulsified oil, or grease (Arya and Philip, 2016).

Among the available options, composite nanomaterials as adsorbents (nanoadsorbents) are expected to overcome these challenges by reducing transport barriers and increasing surface area (Crini, 2003; Liu et al., 2016). Several authors reported that composite materials have a better

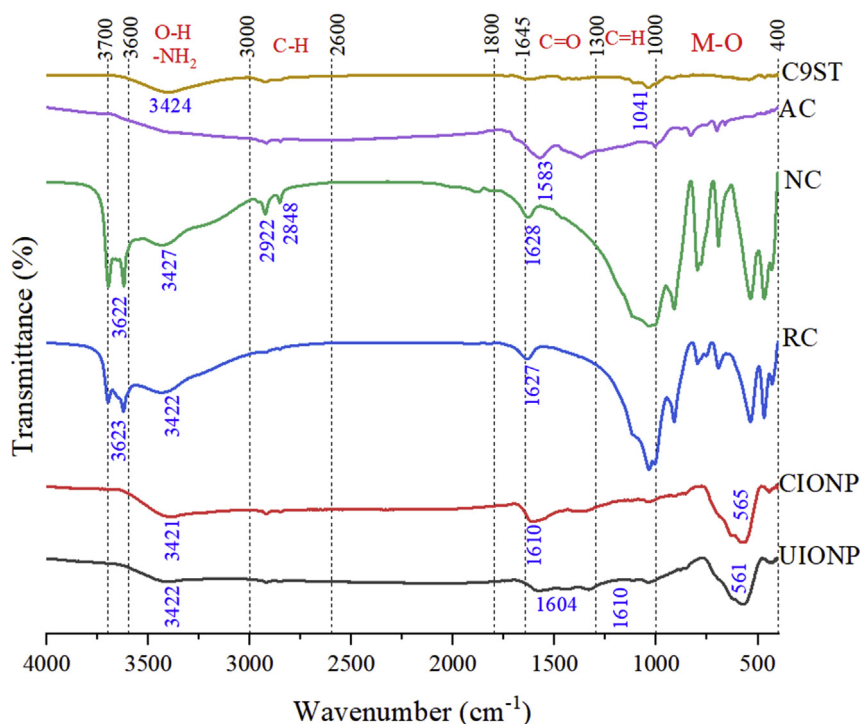


Figure 3. FTIR spectrum of the constituents and PNC (C9ST). Where M = metals (M = Zn, Al, Mg, Ni, and Fe).

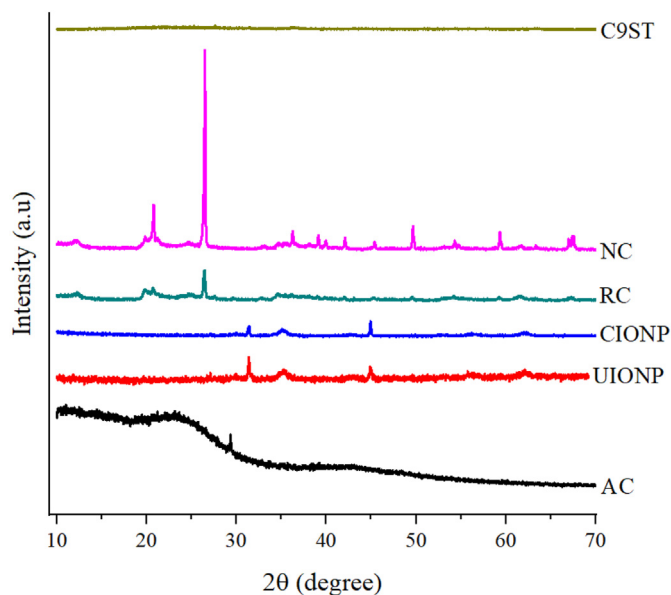


Figure 4. XRD pattern of constituents: activated carbon (AC), uncoated iron oxide nanoparticle (UIONP), coated iron oxide nanoparticle (CIONP), raw clay (RC), nanoclay (NC), and C9ST.

advantage than single nanomaterials but with several limitations such as stability, economic feasibility, and applicability (Zhang et al., 2015). Therefore, research is ongoing to develop novel PNCs adsorbents from biopolymer/AC/NC or modify the existing adsorbents to improve the phosphate removal capacity. The development of such material is a current research hotspot.

Starch has been studied as low-cost emerging adsorbent material (Delval et al., 2003). Starch is a mixture of two polyglucans (amylopectin and amylose) and only contains D-glucose linked by  $\alpha$  1–4 and  $\alpha$  1–6 glycosidic bonds. Starch polymer composites attract most researchers

due to their unique features such as a natural polymer, widely available in different countries, inexpensive, biodegradability, polyfunctionality, high chemical reactivity, and adsorption capacity (Begum et al., 2016). Starch hydrophilicity is a major constraint for developing starch-based materials. Hence, creative modification of the chemical and physical properties or mixing with other chemicals has been experimented with to produce water-resistant adsorbent applicable for various purposes (Crini, 2006; Lu et al., 2009). Cationic corn and potato starch with 1.34 and 0.82 degrees of substitution remove 33% and 29% of TP from wastewater, respectively (Anthony and Sims, 2013). After  $\text{FeCl}_3$  treatment, starch-based flocculants efficiently (90%) remove phosphorus from turbid water (Ren et al., 2020). It might be better to combine  $\text{FeCl}_3$  and starch to reduce workload. However, starch-based PNCs are a new class of adsorbent but rarely reported for phosphate removal. The novel research question of this paper is, what if the plastic materials adsorb pollutants and degrade after disposal rather than a burden to ecology? To answer, an attempt was made to develop plasticized magnetic starch PNC decorated with common water filter media such as AC and NC.

This study aims to develop magnetized bio-plasticized materials to remove dissolved phosphate from synthetic aqueous solutions and raise the notion of bioplastic materials for environmental pollution remedial (Scheme 1). In most cases, the plastic materials fate is disposal to the water bodies and terrestrial environment. In addition, the future might be more dependent on sustainable adsorbents, which originated from renewable biomaterial, the production process, and the adsorbent being eco-friendly. This study was conducted on plasticized magnetic starch-based  $\text{Fe}_3\text{O}_4$  clay PNC to remove phosphate ions from an aqueous solution. The synthesized PNC betterment was compared with the constituent (CIONP).

## 2. Materials and methods

### 2.1. Reagents and materials

Ferric chloride hexahydrate ( $\text{FeCl}_3 \cdot 6\text{H}_2\text{O}$ ) and ferrous chloride tetrahydrate ( $\text{FeCl}_2 \cdot 4\text{H}_2\text{O}$ ) were purchased from Xilong Scientific Co. Ltd., China. Citric acid monohydrate ( $\text{C}_6\text{H}_8\text{O}_7 \cdot \text{H}_2\text{O}$ , ACS grade, 99–102%)

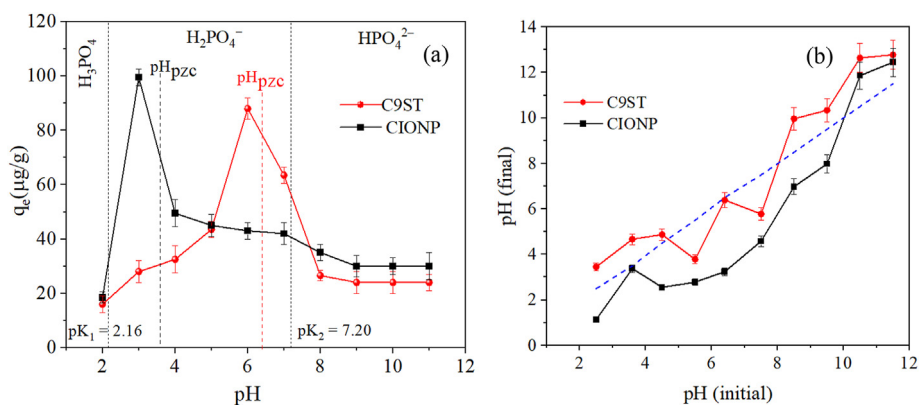


Figure 5. The (a) effect of pH on the adsorbents and (b) point of zero charge (pzc).

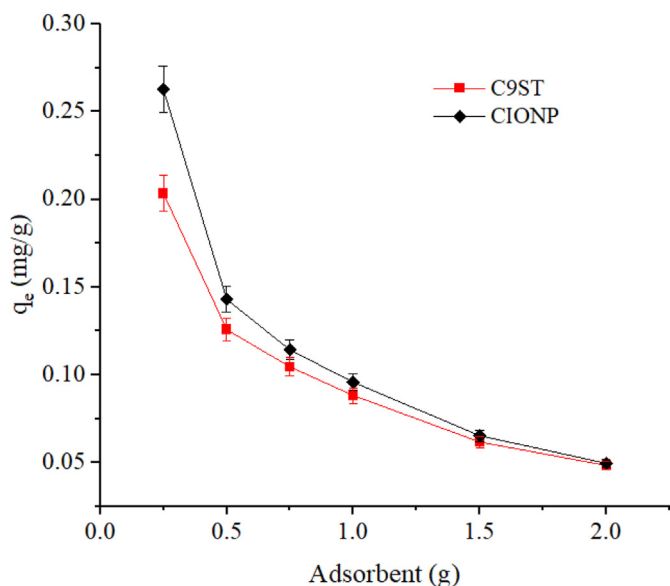


Figure 6. Effect of adsorbent dose.

and sodium hydroxide (NaOH) (98%) were purchased from Neolab and Loba Chemie Ltd., India, respectively. Potassium dihydrogen phosphate ( $\text{KH}_2\text{PO}_4$ ), glutaraldehyde (GA), and Cetyltrimethylammonium bromide (CTAB) were obtained from Sigma-Aldrich Co., MO, USA. Potato starch with amylopectin to amylose weight ratio of 77/23 was supplied from AVI Chem™, Mumbai, India. Glycerol (98% purity) was supplied from CDH® Ltd., India. All the chemicals and reagents were analytical grade.

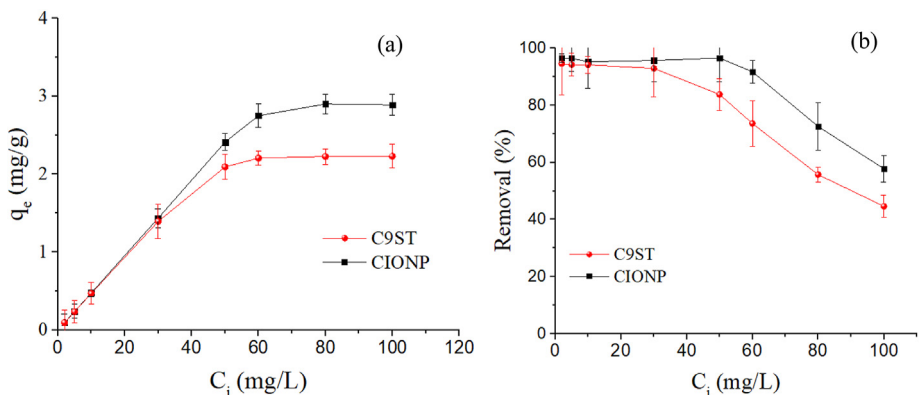


Figure 7. The (a) effect of initial phosphate concentration and (b) phosphate removal efficiency. C9ST = G-plasticized magnetic starch composite and CIONP = coated iron oxide nanoparticle.

## 2.2. Synthesis procedure

### 2.2.1. PNC constituents synthesis

AC was synthesized from the corncob. It was dried in the open air, ground, and sieved (0.05 mm) powder was placed in the muffle furnace at  $450\text{ }^\circ\text{C}$  for 2 h. Then cooled to room temperature for 3–5 h. The activation was carried out by impregnating a 100 g of carbonized corncob with KOH (10% wt.) in 100 mL distilled water solution in a ratio of 1:2 (w/w) until it forms a paste (Tay et al., 2009). The paste was oven-dried at  $105\text{ }^\circ\text{C}$  for 1 h followed by carbonization at  $450\text{ }^\circ\text{C}$  for 1 h (Gratiso et al., 2008). The AC was washed and filtered several times using distilled water to remove excess KOH until the filtrate pH reached neutral (pH 7).

NC was prepared from pristine montmorillonite (MMT) clay soils. The physicochemical analysis of red and black raw clay soils is presented in Table 1. The red and black clay soils texture (clay content) were heavy (85%) and sandy clay (37%) type, respectively, while the pH was nearly similar. Therefore, red clay soil was used for PNC synthesis. The black clay soils CEC were ( $\sim 20$  meq/100g soil) higher than red clay soils. The observed clay soils CEC values were within the previously reported range (De Castro et al., 2019). NC was prepared through the ion exchange method described in Manocha et al. (2008) and Shirsath et al. (2011). A required amount of MMT clay was mixed with 2 mL of HCl in 100 mL of deionized water and heated at  $70\text{ }^\circ\text{C}$  for 1 h. Cetyltrimethylammonium bromide (CTAB) 100% of clay CEC was mixed into the MMT-containing solution. The content was stirred for 12 h at  $70\text{ }^\circ\text{C}$ . The unreacted amines were removed through continuous washing with hot deionized water. The precipitate was oven-dried at  $80\text{ }^\circ\text{C}$  for 24 h and ground using mortar and pestle.

IONPs were synthesized based on the co-precipitation technique (Ali et al., 2017; Kurtan et al., 2015), and the coating methodology was

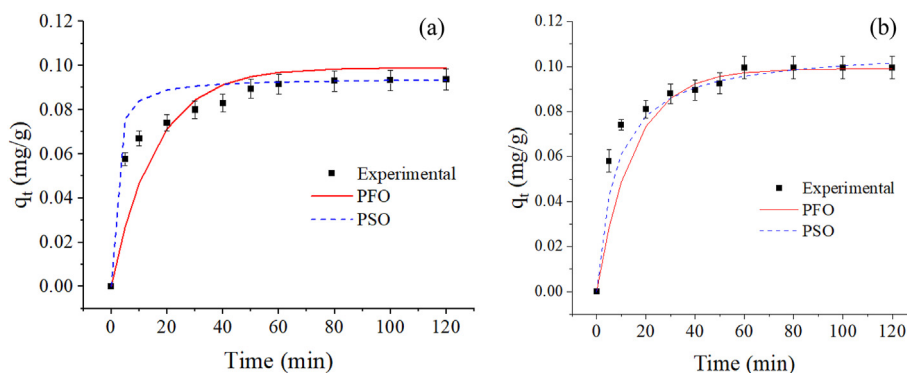


Figure 8. Kinetic analysis of (a) CIONP and (b) C9ST to pseudo-first-order (PFO) and pseudo-second-order model (PSO).

Table 2. Derived parameters of kinetic models.

Adsorbent	$q_e$ (expt) (mg/g)	Pseudo-first-order			Pseudo-second-order			Intra-particle diffusion	
		$R^2$	$q_e$ (cal) (mg/g)	$k_1$ ( $\text{min}^{-1}$ )	$R^2$	$q_e$ (cal) (mg/g)	$k_2$	$R^2$	$k_p$
CIONP	0.089	0.971	0.038	0.043	0.997	0.090	0.337	0.821	0.011
C9ST <sup>a</sup>	0.099	0.972	0.042	0.039	0.998	0.097	0.367	0.841	0.012

<sup>a</sup> G-plasticized magnetic starch-based  $\text{Fe}_3\text{O}_4$  clay polymer nanocomposite.

Table 3. Parameters of isotherm models for the phosphate ion adsorption.

Adsorbent	Langmuir			Freundlich			
	$K_L$	$q_{\text{max}}$ (mg/g)	$R^2$	$R_L$ (L/mg)	$K_F$	$1/n_f$	$R^2$
CIONP	0.068	3.38	0.956	0.326	0.328	0.879	0.995
C9ST	0.094	2.31	0.955	0.323	0.360	0.822	0.997

followed according to Liu et al. (2018) with some modifications. First,  $\text{FeCl}_3 \cdot 6\text{H}_2\text{O}$  and  $\text{FeCl}_2 \cdot 4\text{H}_2\text{O}$  (2:1) were dissolved in 100 mL of distilled water. Then, the solution was dropwise added into a three-neck round-bottom flask with NaOH (2 M). The mixture was stirred at 80 °C using a digital hot plate. The black IONP precipitate obtained at this step was called uncoated iron oxide nanoparticles (UIONP). It was followed by adding a 10 mL solution of 0.5 g  $\text{mL}^{-1}$  citric acid (CA) and vigorous stirring for 30 min. All the reactions were carried out under the  $\text{N}_2$  atmosphere. Finally, the magnetic CA-coated iron oxide nanoparticles (CIONPs) were separated from the solution by magnetic decantation and washed using distilled water to remove impurities. CIONPs were dried in

an oven at 105 °C for 24 h, then ground using mortar and pestle, and stored in rubber capped glass bottles till used in this study.

### 2.2.2. PNC synthesis

The PNC pellets were fabricated according to Arya and Philip (2016) with certain modifications. First (a),  $\text{Fe}^{3+}/\text{Fe}^{2+}$  (x g) in a 2:1 ratio was mixed with NC (z g) in 100 mL distilled water using a magnetic stirrer at room temperature. Secondly (b), the above mixture was slowly added to NaOH (2 M) in a three-neck round bottom flask under vigorous stirring until the pH of the solution reached 9–11 to form iron/NC. Thirdly (c), the required amount of iron-coated clay and powdered AC (a) was dissolved in 100 mL distilled water. It was mixed with the previously prepared solution (first step) to form an iron/NC/AC mixture. Fourth (d) techniques described in Begum et al. (2016) and Cheviron et al. (2015) were adopted with certain alter. 2% (w/v) of powder potato starch was added to 20% (w/v) glycerol (G). Semitransparent Starch/Glycerol (SG) aqueous solution was obtained under constant stirring and heating at a gelatinization temperature of 70 °C for 30–45 min. The above iron/NC/AC (c) solution was added dropwise to 2% w/v SG solution under vigorous stirring for 1 h to form iron/NC/AC/SG. The final step (e) was palletization in the presence of glutaraldehyde (GA) as a cross-linking

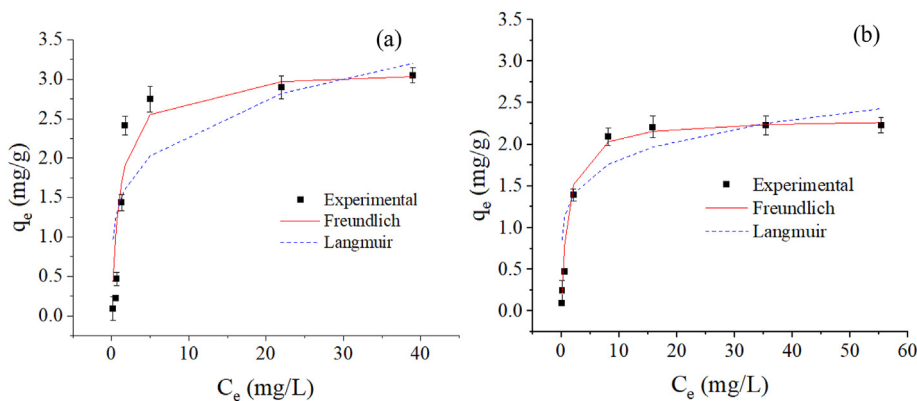


Figure 9. Adsorption isotherm model fit to the (a) CIONP and (b) C9ST phosphate adsorption as a function of initial concentration (2–100 mg/L), pH (3–6), stirred for 1 h at 150 rpm and room temperature ( $25 \pm 1$  °C).

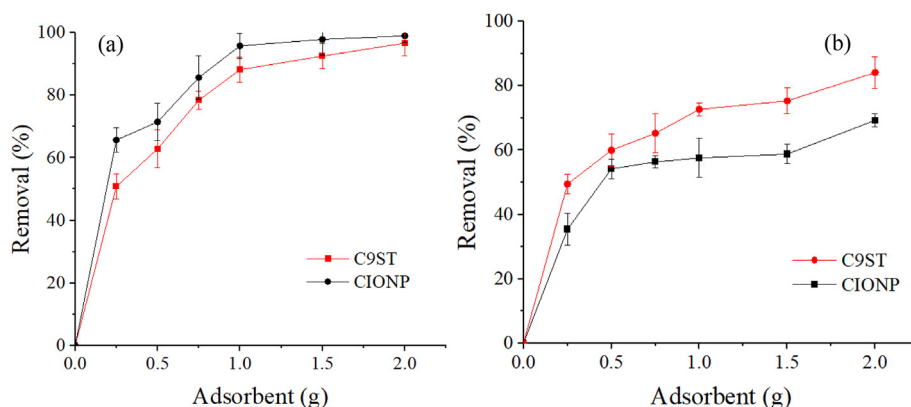


Figure 10. Phosphate adsorption by (a) synthetic and (b) domestic wastewater. Error bars indicate standard deviation.

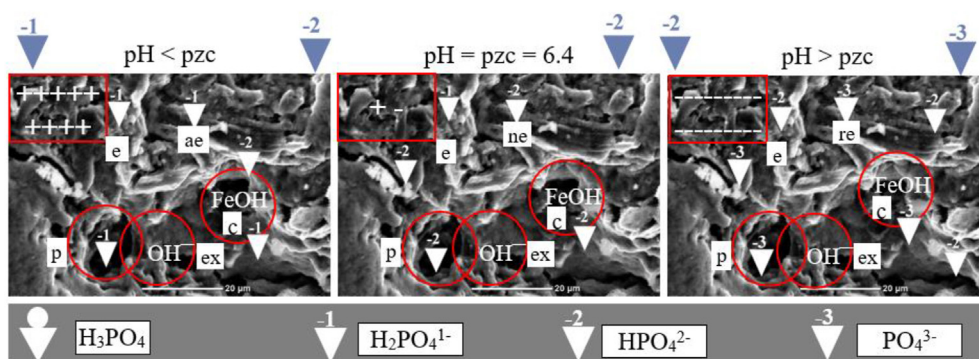


Figure 11. The proposed C9ST phosphate ion adsorption mechanisms with SEM image in the background. where, e = electrostatic, ex = exchange (ligand or ion), c = complexation (inner or outer sphere), p = physisorption, ae = attractive electrostatic force, ne = no (nil) electrostatic attraction force, and re = repulsive electrostatic force and competing with hydroxide (OH<sup>-</sup>) ion. The phosphate species at pH < pzc = pH = 6.4 < pH indicate the dominant spp., see Scheme 2 (supporting information) for details.

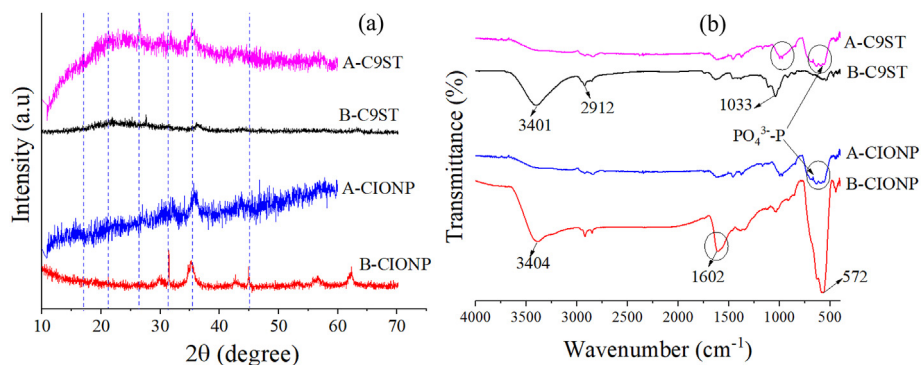


Figure 12. The adsorbents (a) XRD and (b) FTIR spectra before (B-CIONP and B-C9ST) and after (A-CIONP and A-C9ST) phosphate adsorption.

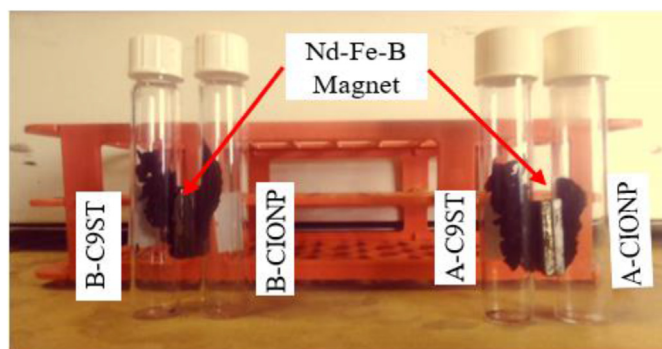


Figure 13. Nd-Fe-N magnet test before (B-C9ST and B-IONP) and after (A-C9ST and A-IONP) phosphate adsorption.

agent (c g), and the GA solution was prepared in distilled water (1% w/v). The GA solution pH was adjusted to 9 using 0.1 M HCl and NaOH. Iron/NC/AC/SG was added dropwise to GA solution from the separatory funnel to form a PNCs plate. After 24 h, it was washed several times using deionized water and oven-dried at 60 °C for 24 h. The NC/polymer/AC/IONP mixing ratio was selected as 1.0/0.5/0.3/0.3 based on Arya and Philip (2016) with modification. C9ST stands for G-plasticized magnetic starch-based PNCs synthesized at GA solution pH 9.

### 2.3. Adsorbent characterization

The raw clay soil was characterized for pH (ISO 10390: 2014), electrical conductivity (ISO 11265: 2014), organic matter (Walkely-Black), total nitrogen (Kjeldahl), cation exchange capacity (ammonium acetate), and calcium carbonate (acid neutralization). UV-Vis absorption studies were conducted using a spectrophotometer (DR 6000, HACH, USA) at 200–900 nm wavelength with a 1 nm scanning step. The crystalline

**Table 4.** Comparison of phosphate adsorption capacity of various adsorbents.

Adsorbent	pH	C <sub>i</sub> (Dose) Sol.	Stir (Kin.) Iso.	MPAC (T)	References
Magnetic IONP	2	2 (0.6) 30	24 h (PSO) F/R	5.03 (25)	Yoon et al. (2014)
Magnetite (MP)	3	0.5 (0.12) 50	2 h (-) -	3.2 (20)	Pan et al. (2010)
Fe <sub>3</sub> O <sub>4</sub> @mZrO <sub>2</sub>	6.9–7	0-300 (0.6) 50	24 h (PSO) L	39.1 (25)	Sarkar et al. (2010)
Iron-Zeolite A	≤10	6 (0.1–4) 500	1 h (PSO) L	2.16 (25)	Saifuddin et al. (2019)
MG@La	5–7	5-200 (40) 40	1.3 h (PSO) E*	116.3 (25)	Nodeh et al. (2017)
ZnOBBNC	7	10 (3) 50	0.25 h (PSO) L	265.5 (25)	Nakarmi et al. (2020)
AC	5	6-25 (40) 40	2.5 h (PSO) F/L	3.02 (25)	Hussain et al. (2011)
AC	6	10-140 (5) 25	24 h (PSO) L	8.69 (25)	Kilpimaa et al. (2015)
ACR	6	10-140 (5) 25	24 h (PSO) L	30.21 (25)	Kilpimaa et al. (2015)
B-Zn/Al-LDH	5	10-200 (0.1) 40	12 h (Elov) L/F	152.1 (25)	Yang et al. (2019)
La2Bent	6	100 (150) 50	24 h (PSO) L	17.86 (25)	De Castro et al. (2019)
Chitosan/Fe <sub>3</sub> O <sub>4</sub>	7	2 (6 g) 50	24 h (PSO) L/F	0.96 (25)	Waweru et al. (2019)
Chitosan/Zr	3	10-30 (800) 50	0.33 h (PSO) L	71.68 (25)	Liu et al. (2016)
Chitosan Fe (III)	3	50 (1 g) 100	48 h (PSO) F	15.58 (25)	Zhang et al. (2015)
Chitosan beads	5	10-180 (-) -	6.67 h (Both) L	28.86 (25)	Dai et al. (2011)
MCCS	6.8	100 (100) 50	1.25 h (PSO) L	22.88 (25)	Fan and Zhang (2018)
FeCl <sub>3</sub> + Starch*	5	2.5† (100) 100	0.8 h (-) -	0.59 (25)	Ren et al. (2020)
FeCl <sub>3</sub> + Starch*	7	2.5† (100) 100	0.8 h (-) -	2.77 (25)	Ren et al. (2020)
Corn C-starch	7	4 (-) -	1.17 h (-) -	1.32 (25)	Anthony and Sims (2013)
Potato C-starch	7	4 (-) -	1.17 h (-) -	1.16 (25)	Anthony and Sims (2013)
CIONP	3	2-100 (1) 50	1 h (PSO) F/L	3.12 (25)	This study
C9ST	6	2-100 (1) 50	1 h (PSO) F	2.31 (25)	This study

pH = optimum pH, C<sub>i</sub> (Dose) Sol. = initial P concentration (mg/L) (adsorbent dose, g) solution in mL, stir (Kin.) Iso. = optimum stirring time (h) (kinetics best fit) isotherm best fit, MPAC = maximum phosphate adsorption capacity, C-starch = cationic starch, PFO = pseudo-first-order model, PSO = pseudo-second-order model, Both = PFO and PSO, Both\* = Langmuir and Freundlich, Elov = Elovich kinetics model, L = Langmuir, F = Freundlich, R = Redlich–Peterson, \*St-CTA = a cationic starch with quaternary ammonium salt (CTA) added after FeCl<sub>3</sub> application (separately), MCCS = modified cellulose from corn stalks and † = TP, MG@La = lanthanum hydroxide doped onto magnetic reduced graphene oxide, E\* = free energy, IONP = iron oxide nanoparticle, NC = nanoclay, and CIONP = coated iron oxide nanoparticle, C9ST = starch-based Fe<sub>3</sub>O<sub>4</sub> clay polymer nanocomposite, La2Bent = lanthanum (III) modified montmorillonite.

structure was examined using X-ray diffraction (Bruker D8, Bremen, Germany) with a Cu K $\alpha$  source ( $\lambda = 1.5406 \text{ \AA}$ ) from  $10^\circ$  to  $70^\circ$  ( $2\theta$ ) at a scanning rate of  $2^\circ \text{ min}^{-1}$ . The functional groups were studied by FTIR spectroscopy (Spectrum 65, PerkinElmer, USA) in the range of  $400\text{--}4000 \text{ cm}^{-1}$  with a resolution of  $4 \text{ cm}^{-1}$  using KBr pellets. The samples were analyzed in the powder form (ATR) technique. The pH value was measured by a multi pH meter with a resolution capacity of pH 0.001–0.1 (HQ440D, HACH, USA). The adsorbent surface morphology was examined using Scanning Electron Microscopy (SEM) operating at 15 kV (JCM-6000Plus, JEOL Ltd., Japan). The SEM images were analyzed using ImageJ software (v1.53k).

#### 2.4. Batch adsorption experiment

The adsorption of phosphate ions was studied using the batch method. The synthetic stock phosphate concentration was prepared according to APHA (2005) by dissolving 219.5 mg anhydrous KH<sub>2</sub>PO<sub>4</sub> in 1 L deionized water ( $1.00 \text{ mL} = 50.0 \mu\text{g PO}_4^{3-}\text{-P}$ ), then a working solution was prepared through dilution. The adsorption capacity of adsorbate (phosphate ions) on the adsorbents (CIONP and PNC) was studied as a function of pH, adsorbent dose, reaction time (kinetics), and initial phosphate concentration (isotherm) (Waweru et al., 2019; Yoon et al., 2014). The parameters effect was studied in terms of pH (2–11), initial P concentration (2–100 mg/L), adsorbent dose (0.25–2 g), and contact time (5–120 min). The solution pH was adjusted using 0.1 M NaOH and HCl. The experimental data were fitted into the kinetics and isotherm model. All the experiments were carried out in a 250 mL capped Erlenmeyer flask at 150 rpm and room temperature ( $25 \pm 1^\circ \text{C}$ ). After a specified contact time (t), the adsorbents were separated with the aid of a

magnet. Then, the supernatant solution was filtered through a  $0.45 \mu\text{m}$  Whatman membrane filter paper, and the filtrate was collected for phosphate concentration analysis (C<sub>f</sub>). In addition, the adsorbents were tested in batch mode using real domestic wastewater (WW). The WW was collected from a primary clarifier at Mickey Leland condominium domestic WW treatment plant (Asko, AA, Ethiopia). The batch experiments were conducted in duplicate.

#### 2.5. Analytical methods

In all adsorption experiments, the initial and final phosphate concentration was determined using the ascorbic acid method (4500-P E) described in APHA (2005). Ultraviolet-Visible (UV-Vis) spectrophotometer (DR 6600, HACH, USA) was used to determine the phosphate concentration (mg/L) in a sample solution at 880 nm wavelength. The calibration curve with a minimum of five points was plotted routinely to calculate the phosphate concentration. The analytical instruments and tools were calibrated before the day's measurements. The point of zero charge (pzc) was determined through the modified salt titration method (Tan et al., 2008). It was measured by adding 0.2 g of adsorbent into 20 mL of 0.1 M KCl in various 50 mL tubes. Then, the mixed solution initial pH (pH<sub>i</sub>) was adjusted to pH 2–11 using 0.1 M HCl and NaOH. Each tube was agitated for 24 h continuously at room temperature; after settling, the pH was measured again to get the final pH (pH<sub>f</sub>). The  $\Delta\text{pH}$  (pH<sub>f</sub>–pH<sub>i</sub>) was calculated and plotted against the initial pH. Hence, the initial pH at which  $\Delta\text{pH} = 0$  is taken as pzc. The materials physicochemical characteristics were analyzed: Cation Exchange Capacity (CEC) (Ammonium Acetate Distillation), pH (ES ISO 10390: 2014 (1:2.5)), Calcium Carbonate (CaCO<sub>3</sub>) (acid Neutralization), organic matter (Walkely and

Black), total nitrogen (TN) (ES ISO 11261:2015, Kjeldahl Method), Electrical Conductivity (EC) (ES ISO 11265: 2014 (1:5), and Bulk Density (oven dry).

## 2.6. Calculations

The  $\text{PO}_4^{3-}$ -P adsorption capacity (mg of adsorbate/g of adsorbent) at any time ( $q_t$ ) and equilibrium ( $q_e$ ) was calculated by Eqs. (1) and (2), respectively (Li et al., 2018). The phosphate removal efficiency of each adsorbent was calculated according to Eq. (3).

$$q_t = (C_0 - C_t) \left( \frac{V}{m} \right) \quad (1)$$

$$q_e = (C_0 - C_e) \left( \frac{V}{m} \right) \quad (2)$$

$$R(\%) = (C_0 - C_t) \left( \frac{100}{C_0} \right) \quad (3)$$

where  $q_t$  and  $q_e$  (mg/g) are the removal capacity at any time (t) and equilibrium, respectively; R (%) shows the removal efficiency;  $C_0$ ,  $C_t$ , and  $C_e$  (mg/L) are for adsorbate (phosphate ion) initial concentration, any time t (min), and equilibrium, respectively; V (L) is the volume of solution, and m (g) is adsorbent mass.

## 3. Results and discussion

### 3.1. Characterization of adsorbents

#### 3.1.1. Surface morphology

SEM was utilized to examine the surface morphology of the G-plasticized magnetic starch-based polymer nanocomposite (C9ST). Figure 1d illustrates that the synthesized PNC was flexible after drying for 24 h in the oven at 60 °C Figure 1a and b show SEM micrographs of the fabricated PNC before and after phosphate adsorption, in turn. The SEM microimages of C9ST magnified 1500X showed a sheet-like heterogeneous porous surface morphology. The C9ST before phosphate adsorption reveals a maximum pore size of 16  $\mu\text{m}$  with an average of  $\sim 11 \pm 6 \mu\text{m}$  (Figure S5), but the pores were not visible after the adsorption test (Figure 1b). It could be due to phosphate ions adsorption. In contrast, Tarique et al. (2021) observed homogeneous surfaces from G-plasticized starch-based films without adsorbents. Hence, the heterogeneity of the C9ST surface could be due to the admixed adsorbents. It is expected that heterogeneity may affect the surface tensile property. On the other hand, it may accelerate the degradation process, which could be a subject of additional studies.

#### 3.1.2. Ultraviolet-Visible (UV-Vis) spectroscopy analysis

As shown in Figure 2, the absorbance peaks at 200–250 nm were observed in the constituents. A sharp peak was observed in CIONP at 224 nm. The RC and NC reveal a similar adsorption band range. However, the RC peak pattern at 220 nm resembles PNC. It signals the RC may contain organic polymer (starch) from biomass contamination, which could be removed during the RC cleaning process. In C9ST, the absorbance band peak was observed at 247 nm and slightly declined to 385 nm. Similarly, Krystyan et al. (2021) noted a peak at about 233 nm and a wider band at 290–305 nm while studying Starch/Chitosan polymer nanocomposite. The absorbance band peaks at 220 nm (C=O) (Kavitha, 2017), 227 nm (C-C aromatic bonds) (Ahmad, 2019), and 230–235 (C=C) (Krystyan et al., 2021) arose due to  $\pi \rightarrow \pi^*$  transition. The peak at 297–300 nm is associated with  $n \rightarrow \pi^*$  transition of C=O bonds (Ahmad, 2019; Krystyan et al., 2021). According to Kavitha (2017) the  $\pi \rightarrow \pi^*$  transition at 220 nm attributed with C=O group occurs due to starch polymer degradation. The absorption band increase and peak shift when the starch polymer was incorporated into the C9ST matrix signals the association of

constituents with the starch polymer. The previous studies also noted that the UV-Vis spectra peak shift implicates the proper synthesis of polymer nanocomposite (Kavitha, 2017; Krystyan et al., 2021).

#### 3.1.3. Fourier transforms infrared (FTIR) spectroscopy analysis

FTIR spectroscopy was used to study the PNC and constituents' surface functional groups. According to Figure 3, the wide IR spectra band at 3600-3000  $\text{cm}^{-1}$  were related to the hydroxyl group's vibration band (-OH) in all materials. Similar findings were reported by (Bhatia et al., 2017; Nordin et al., 2020). The OH and amine related peaks between 3700-3600  $\text{cm}^{-1}$  and 3442-3360  $\text{cm}^{-1}$ , respectively, were revealed in RC and NC, whereas in NC a new peak at 2848 and 2922  $\text{cm}^{-1}$  were associated with the methyl (C-H) group from the CTAB modification. It implies the CTAB was effectively grafted on NC. These agree with IR analysis reported in previous studies (Bhatia et al., 2017; Tarique et al., 2021; Manocha et al., 2008). Based on Eng et al. (2013), the peak at 1645 shows the water OH deformation. The peaks band between 1000 to 400  $\text{cm}^{-1}$  are related to metal-oxygen bond (M-O and O-M-O), where M = Zn, Al, Mg, Ni, and Fe (Yang et al., 2019). The peaks were shallow in C9ST that suggests the constituents were incorporated into the polymer matrix. In contrast, its significant absorption peak in CIONP/UIONP is attributed to  $\text{Fe}^{2+} \leftrightarrow \text{O}$  and  $\text{Fe}^{3+} \leftrightarrow \text{O}$ , compared with Maity and Agrawal (2007) assigned IR spectra it shows the formation of  $\text{Fe}_2\text{O}_4$  or  $\text{Fe}_3\text{O}_4$  nanostructures and proves Fe-O vibration. The FTIR result confirmed that there are functional groups in the nanoparticle structure. These changes in the IR spectrum show that the nanoparticles have been successfully synthesized.

As shown in Figure 3, the FTIR spectra of PNC show a peak at 3424  $\text{cm}^{-1}$ , 3391  $\text{cm}^{-1}$ , 2922  $\text{cm}^{-1}$ , 1729  $\text{cm}^{-1}$ , 1643  $\text{cm}^{-1}$ , 1034  $\text{cm}^{-1}$ , and 815  $\text{cm}^{-1}$  are related to  $-\text{NH}_2$ , O-H vibration, C-H, C=O, O-H stretching, C-OH, and C-OC stretching, respectively. The IR spectra interpretation is supported by Nodeh et al. (2017). These O-H peaks are related to the hydroxyl group of the absorbed water and glycerol used to plasticize starch, as supported by the findings of Tarique et al. (2021). The C-O stretching vibration band higher than 993  $\text{cm}^{-1}$  is related to starch and glycerol polysaccharide compounds (Syafiq et al., 2021). Magnetic stretching observed at 575  $\text{cm}^{-1}$  (Fe-O) reveals the proper PNC magnetization. The overall observed FTIR evidence supports the possible plasticized magnetic starch-based  $\text{Fe}_3\text{O}_4$  clay composite synthesis.

#### 3.1.4. Powder X-ray diffraction (XRD) analysis

The adsorbents mineralogical composition and crystalline structure were studied by X-ray diffraction. Figure 4 shows the XRD pattern of constituents and PNC. The XRD pattern reveals a well-defined crystalline structure of the materials except for AC. In AC, the broad peak at  $2\theta = 23^\circ$  and  $43^\circ$  confirms the amorphous structure, which is in accordance with the literature (Juang et al., 2018). The XRD analysis of AC does not reveal a sharp signal due to its amorphous structure (Boki et al., 1987). The XRD result of CIONP shows a peak at  $2\theta = 31.4^\circ$ ,  $35.0^\circ$ ,  $44.9^\circ$ , and  $62.0^\circ$ , while UIONP peaks observed at  $53.0^\circ$ ,  $55.8^\circ$  and  $62.1^\circ$ , which proves the  $\text{Fe}_3\text{O}_4$  crystal structure formation and agree with the Joint Committee for Powder Diffraction Standards (JCPDS) card No. 19-0629 (Sandhya and Kalaiselvam, 2020). The XRD pattern for PNC presents a sharp peak at  $26.2^\circ$  (Figure 4). It signals the NC was loaded into the PNC. A similar pattern was reported in the previous study (Eng et al., 2013; Nodeh et al., 2017).

### 3.2. Effect of pH

The pH is an important parameter that affects the adsorption process (Battas et al., 2019). Figure 5a shows that the adsorption capacity increases until climax and is followed by a decrease with an increase in pH value for all adsorbents. The effect of pH on phosphate adsorption was studied over a wide range (pH = 2–11) with 20 g/L adsorbents in 50 mL of 2 mg P/L solution and stirred for 1 h. The initial phosphate concentration (2 mg/L) and adsorbent dose (1 g) were selected (to start the

optimization experiment) based on previous studies on related adsorbents (Waweru et al., 2019; Yoon et al., 2014). The optimum constituent phosphate adsorption was recorded at acidic pH (3), while PNC at slightly acidic (pH = 6). In agreement, the pzc of CIONP and C9ST were observed at pH = 3.6 and 6.4, in turn (Figure 5b). The PNC potentially reduces the time and energy required to raise the raw domestic wastewater pH, often near neutral (Metcalf and Eddy, 2014). All other parameters were studied at each optimum adsorbent pH. It agrees with Hussain et al. (2011) that noted AC adsorption capacity occurs at pH ≤ 5 but declines as the pH increases; however, limestone addition pulls the optimal pH value to neutral (pH = 7). Similarly, Yoon et al. (2014) showed that the IONP phosphate adsorption decreases as the pH increases from 2-6.

The optimum phosphate adsorption pH varies among the adsorbents. It indicates that certain factors contribute to the pH effect. Multiple nanoparticles might decrease the acidic pH selectivity (favorable) for phosphate adsorption in the PNC than constituents. The adsorption nature may be explained by the surface chemical and solution pH properties. Starch contains carboxyl and -OH groups, CIONP (-OH), AC (-OH and carboxyl), while NC has amine groups (-NH<sub>2</sub>) through organo-modification (Jiang et al., 2013; Juang et al., 2018; Krystijan et al., 2021). The solution pH affects the adsorbent surface and determines the phosphate species (Liu et al., 2016). The electrostatic force between the adsorbents and phosphate ion depends on pH: at pH < 2.1 (H<sub>3</sub>PO<sub>4</sub>) no attraction, pH 2.1–7.2 (H<sub>3</sub>PO<sub>4</sub><sup>-</sup>) and pH 7.2–12 (H<sub>3</sub>PO<sub>4</sub><sup>2-</sup>) attraction, and at pH > 12 (PO<sub>4</sub><sup>3-</sup>) competing with -OH (Nodeh et al., 2017). The optimal adsorption pH variation could arise mainly due to the electrostatic repulsion or attraction between the functional groups at the adsorbent's surface and negatively charged phosphate ions.

### 3.3. Effect of adsorbent dose

Varying adsorbent doses (0.25–2 g) effect on phosphate adsorption was studied under 50 mL solution with 2 mg P/L at each adsorbent's optimum pH value, while other conditions were kept constant as described before. Figure 6 shows a declining phosphate adsorption capacity (q<sub>e</sub>) trend as the adsorbent dose increases. The CIONP dose of 0.25–2 g (5–40 g/L) in 2 mg P/L treated about 0.14–0.21 mg P/g, but under similar conditions, the PNC could adsorb 0.04–0.26 mg P/g. When the adsorbent dosage increased, the phosphate removal percentage increased, but higher doses had little effect. It indicates that the amount of phosphate adsorbed by the adsorbents is inversely proportional to the adsorbent dose. The available active site for adsorption might increase with increasing adsorbent dose. However, the extra addition of adsorbent dose reduces the adsorption capacity, despite increasing the available active sites. It is probably due to the available amine, carboxylic, or active oxide sites being initially high at lower adsorbent dosage, but as the adsorbent dose increases simultaneously particles aggregate that reduces adsorption efficiency (Battas et al., 2019).

### 3.4. Effect of initial concentration

The effect of initial phosphate concentration (2–100 mg P/L) was studied at the adsorbent's optimal pH, whereas keeping other conditions constant. The CIONP and PNC equilibrium initial concentrations were 50 and 35 mg/L, in turn (Figure 7a). When the phosphate concentration was increased from 2 to 100 mg P/L, the phosphate adsorption capacity was increased in CIONP (0.1–2.89 mg P/g) and PNC (0.1–2.23 mg P/g). Similarly, Fan and Zhang (2018) showed that increasing phosphate concentration also increases the adsorption capacity. Given the highest optimal adsorption pH in the PNC, a relatively lower (45% at 100 mg P/L) adsorption capacity was observed by PNC. It could be due to the particle's agglomeration in high phosphate concentration. Nanomaterials aggregation is random without defined orientation, mainly due to surface charge (FeO-ICG = -16.9 mv) (Bell et al., 2019). One approach to alter the agglomeration effect is increasing the agitation speed. However, this

collinearly increases energy requirement during the actual water treatment process and makes it difficult for application. Another alternative is modifying the material by blending with other adsorbents, optimizing the constituent ratio, or dispersing the planar clay sheets using organic (inorganic) modifiers. Therefore, it can be concluded that there is a positive synergistic effect between the biopolymer and nanomaterials that form the PNC to adsorb phosphate ions. As shown in Figure 7b, the adsorbents removal efficiency declined with increasing phosphate concentration until equilibrium is achieved. The phosphate ion removal observed in PNC (45-95%) was comparable to the CIONP (58-97%) under initial 2–100 mg P/L phosphate ion concentration. This decline in phosphate removal efficiency could be due to the active adsorbent site saturation. However, 2 mg/L was selected for further study due to the P load in natural water bodies and after secondary effluent was often < 2 mg/L (Waweru et al., 2019).

### 3.5. Adsorption kinetics

Adsorption kinetics was studied to determine the rate of phosphate uptake by the PNC and constituents. Pseudo-first-order (PFO) (Lagergren first-order) (Eq. 4) and pseudo-second-order (PSO) (Ho and McKay, 1999) (Eq. 5) models were used to describe the kinetics of adsorption experiments. Weber and Morris (1963) intra-particle diffusion model was adopted to determine the diffusion mechanism, as shown in Eq. (6).

$$\ln(q_e - q_t) = \ln q_e - k_1 t \quad (4)$$

$$\frac{t}{q_t} = \frac{1}{k_2 q_e^2} + \frac{1}{q_e} t \quad (5)$$

$$q_t = k_p t^{1/2} + C \quad (6)$$

where k<sub>1</sub> is the PFO rate constant, k<sub>2</sub> is the PSO rate constant, q<sub>e</sub> is the adsorbed phosphorus at equilibrium (mg P/g), q<sub>t</sub> is the adsorbed phosphorus (mg P/g) at the time (t), k<sub>p</sub> is the rate constant of intraparticle diffusion (mg P/g.min<sup>1/2</sup>), and C is the liquid-solid layer effect.

The effect of time on the adsorbents was studied using optimum phosphate concentration and adsorbent dose at different contact times (5–120 min) at 150 rpm and room temperature (25 ± 1 °C). In both adsorbents, the adsorption rate was highest within the first 30 min. Meanwhile, the PNC and CIONP reach equilibrium within 60 and 50 min, in turn (Figure 8a and b).

The experimental data obtained as a function of contact time were fitted into the adsorption kinetics model. The phosphate ions adsorption increased as the contact time increases until equilibrium was achieved (Figure 8). However, as the contact time increased further, no more adsorption occurs; this adsorption equilibrium might be due to the saturation of the free adsorbent sites. Additionally, based on the Freundlich model, it could be due to the adsorption binding energy decreases exponentially as the surface saturation increases (Battas et al., 2019).

The PFO kinetic model indicates the adsorption mechanism is due to physisorption, while the PSO implies chemisorption (Saifuddin et al., 2019). Table 2 shows the PSO expresses more the composite and constituent adsorption experimental data due to a higher determination coefficient (R<sup>2</sup> > 0.99) than PFO (R<sup>2</sup> > 0.97). The results suggest that the PNC adsorption process is mainly due to the chemisorption process, as a rate-limiting factor between the phosphate ion and adsorbents through sharing electrons or ion exchange. The intra-particle diffusion model controls the adsorption process if the lines pass through the origin (Jiang et al., 2013). Based on Figure S2, in which the lines do not pass through the origin. Hence, it can be concluded that intra-particle diffusion was not the only adsorption rate-controlling step, and the mechanism involves simultaneous adsorption and intra-particle diffusion. The good linearity of the plots might indicate that intra-particle diffusion may play a significant role during the initial adsorption stage.

### 3.6. Adsorption isotherm

Adsorption equilibrium isotherm data provides valuable information to determine the adsorption process characteristics, the interaction between adsorbate and the adsorbent surface property (Battas et al., 2019; Juang et al., 2018). It explains the function of concentration on the adsorbent surface at constant temperature (Waweru et al., 2019). Adsorption isotherm was tested as a function of initial phosphate concentration. Langmuir and Freundlich isotherm models were applied to determine the phosphate adsorption isotherm test.

The Langmuir model assumes adsorption is a (1) reversible phenomenon on (2) homogeneous monolayer surface without any interaction between adsorbed molecules, and the rate is dependent on (3) the initial adsorbate concentration and (4) available site on the adsorbent. The linearized form ( $C_e/q_e$  vs  $C_e$ ) with slope  $1/q_{max}$  plotted as Eq. (7) (Langmuir, 1917). The essential characteristics of the Langmuir equation can be expressed using a dimensionless equilibrium parameter or separation factor ( $R_L$ ) shown in Eq. (8) (Abukhadra et al., 2020). The process reversibility was evaluated using four possibilities of  $R_L$  value: favorable  $0 < R_L < 1$ , unfavorable  $R_L > 1$ , linear  $R_L = 1$ , and irreversible  $R_L = 0$ .

$$\frac{C_e}{q_e} = \frac{1}{q_{max}} C_e + \frac{1}{q_{max} K_L} \quad (7)$$

$$R_L = \frac{1}{1 + K_L C_0} \quad (8)$$

where  $q_{max}$  is the maximum adsorption capacity (mg/g),  $K_L$  is the Langmuir adsorption constant,  $q_e$  is the adsorbed amount at equilibrium concentration (mg/g),  $C_e$  is the equilibrium concentration (mg/L), and  $C_0$  is the highest initial adsorbate concentration (mg/L).

The Freundlich model is an empirical sorption isotherm for the non-ideal system. This model assumes (1) heterogeneous surface adsorption and (2) the binding energy decreases exponentially with increasing surface saturation. Freundlich linearized form ( $\log q_e$  vs  $\log C_e$ ) plotted and adsorbed concentration per unit adsorbent at equilibrium is given as Eq. (9) (Ho et al., 2005).  $K_F$  and  $n$  were calculated from intercept and slope, in turn. A higher  $K_F$  value indicates the adsorbent has a higher adsorption capacity than adsorbate, and a small  $1/n$  shows the strong adsorption bond (Hussain et al., 2011). The  $n$  value shows the type of adsorption: favorable ( $1 < n > 10$ ), normal ( $1/n < 1$ ), and cooperative ( $1/n > 1$ ) adsorption.

$$\log q_e = \log K_F + \frac{1}{n} \log C_e \quad (9)$$

where  $C_e$  (mg P/L) is liquid-phase phosphate concentration at equilibrium,  $K_F$  is the Freundlich adsorption constant, and  $1/n$  (dimensionless heterogeneity factor) is the Freundlich intensity of adsorbent adsorption.

According to Table 3 and Figure 9, the phosphate ions adsorption onto the PNC and constituent best fit the Freundlich isotherm model ( $R^2 > 0.99$ ). However, the Langmuir model can be applied for the constituents because  $R^2 > 0.95$ . This conclusion was supported by the SEM data (Figure 1a and b) that show the PNC (C9ST) surface was rough and heterogeneous. The Freundlich model assumes the adsorbent surface is heterogeneous and phosphate ion adsorption energy on the adsorbent decrease exponentially with increasing surface saturation (Battas et al., 2019). Based on Langmuir ( $K_L$ ) and Freundlich adsorption intensity ( $1 < n > 10$ ) values, the phosphate adsorption onto the adsorbents was favorable (Nodeh et al., 2017). The CIONP and C9ST MPAC ( $q_{max}$ ) were 3.12 and 2.38 mg P/g, in turn, which is in the range of the reported MPAC of adsorbents (3–476 mg P/g) (Table 3).

### 3.7. Application in real wastewater

The synthesized PNC and constituent (CIONP) were exposed to real domestic wastewater (WW). The WW was filtered and analyzed as

described in analytical method section 2.5. The WW characteristics were  $pH = 7.51 \pm 0.07$ ,  $TP = 9$  mg/L, and ammonia = 35 mg/L. Then, in a separate flask, 0.25–2 g of each adsorbent (CIONP and PNC) was added into 50 mL of WW and stirred for 1 h at 150 rpm and room temperature ( $25 \pm 1$  °C). The adsorbents phosphate removal efficiency from synthetic or real WW applications were compared. The observed results show that the PNC and constituent phosphate removal efficiency was reduced in real WW than synthetic by ~11–16% and ~15–29%, respectively (Figure 10). It might be due to competing ions and complex reactions in the real domestic WW. In domestic WW and most inland water, where pH ranges between 6.5 to 8.5, the most dominant phosphate species are  $H_2PO_4^-$  and  $HPO_4^{2-}$  (Metcalf and Eddy, 2014). Given various factors interfering with the adsorption process, the PNC phosphate adsorption was higher than the constitutions. Similarly, Nodeh et al. (2017) reported 74–90% phosphate removal from the river and real sewage WW using MG@La.

### 3.8. Phosphate adsorption mechanism

Figure 11 and Scheme 1 presents the proposed adsorption mechanisms. The phosphate adsorption mechanisms could be electrostatic interaction and physisorption. It is because phosphate ions being negatively charged over a wide pHs range and C9ST was porous. In support, the FTIR spectra confirmed the peak shift in C9ST (3401, 2912 & 1033  $cm^{-1}$ ) and CIONP (3404, 1602, & 572  $cm^{-1}$ ), which indicates the amine, -OH, and carboxyl groups involvement in the phosphate adsorption process (Figure 12b). SEM images (Figure 1a and b) signal physisorption could be a possible phosphate removal means. It is previously reported that the metal hydroxides remove phosphate ions through inner and surface electrostatic complexations (Nagoya et al., 2019; Nodeh et al., 2017). Literature review shows phosphate adsorption is also possible through ion or ligand exchange (Guibal, 2004; Xie et al., 2014; Yang et al., 2019). In addition, the FTIR spectra show the presence of  $PO_4^{3-}$  and P-OH on the adsorbent at 1070, 960, and 787  $cm^{-1}$ . These IR spectra variations after phosphate adsorption were reported in previous studies (Nodeh et al., 2017; Yang et al., 2019). Overall, the FTIR confirms the successful adsorption of phosphate ions by the adsorbents (CIONP & C9ST). Figure 12a shows the adsorbents (both the constituent (CIONP) and PNC crystalline nature was altered after phosphate adsorption from the synthetic aqueous solution.

Moreover, the adsorbents recovering and restoring characteristics were tested using the Nd-Fe-B magnet approach described in Juang et al. (2018). The Fe-Nd-B magnet attracts the CIONP and C9ST before and after adsorption (Figure 13), showing the possible adsorbent recovery using a magnetic field. It indicates that the G-plasticized starch composite preserves the magnetic properties after adsorption.

### 3.9. Comparison of adsorbents with other studies

The comparison of the synthesized adsorbent with other studies is shown in Table 4. These results indicate that the C9ST had a higher adsorption capacity than cation starch (corn and potato),  $FeCl_3$ , starch, and Chitosan/ $Fe_3O_4$  reported in different studies (Ren et al., 2020; Waweru et al., 2019; Yoon et al., 2014). However, it was lower than magnetic iron oxide nanoparticles and metal-modified adsorbents such as Chitosan/Zr, Chitosan/Cu (II), but their optimal pH is  $\leq 5$  (except  $Fe_3O_4@mZrO_2$ ).

## 4. Conclusions

Plasticized magnetic starch-based  $Fe_3O_4$  clay polymer nanocomposite (PNC) was prepared as an improved adsorbent material to remove phosphate ions from an aqueous solution. The enhancement was stepwise studied by comparing PNC phosphate adsorption with one of the constituents (coated magnetic iron oxide (CIONP) under batch experiment. The study parameters showed that the phosphate ion adsorption

efficiency increased with the adsorbent dose and decreased with the initial phosphate concentration. The maximum phosphate ion adsorption capacity (MPAC) onto the CIONP was observed at acidic media (pH = 3), while the PNC shifted the pH to slightly acidic (pH = 6). Hence, the PNC improvement was observed in terms of enhanced optimal adsorption pH. This achievement favors the PNC application for real domestic wastewater treatment, which mostly operates at near-neutral pH. The CIONP and PNC MPAC were 3.12 and 2.31 mg/g, respectively. The adsorption isotherm data applied to Langmuir and Freundlich model, the results indicate that the Freundlich model best fits the PNC and CIONP. Furthermore, the pseudo-second-order model more describes the adsorption kinetics of the adsorbents. Overall, the results strongly support a positive synergistic effect between plasticized biopolymer (starch) and constituents such as CIONP, NC, and AC to remove phosphate ions from an aqueous solution. Thus, the findings prove that PNC has a potential for phosphate ion removal from an aqueous solution. However, it requires further studies to optimize the adsorbent concentration, modifying the content, bioavailability, and biotoxicity during utilization or after the plasticized materials disposal.

## Declarations

### Author contribution statement

Tesfalem Atnafu: Performed the experiments; Analyzed and interpreted the data; Contributed reagents, materials, analysis tools or data; Wrote the paper.

Seyoum Leta: Conceived and designed the experiments; Analyzed and interpreted the data.

### Funding statement

This work was supported by Center for Environmental Science, Addis Ababa University and Mettu University.

### Data availability statement

Data will be made available on request.

### Declaration of interests statement

The authors declare no conflict of interest.

### Additional information

Supplementary content related to this article has been published online at <https://doi.org/10.1016/j.heliyon.2021.e07973>.

## Acknowledgements

The authors would like to thank Addis Ababa University and Mettu University for providing the necessary equipment and laboratory facilities.

## References

Abukhadra, M.R., Adlii, A., El-Sherbeeny, A.M., Ahmed Soliman, A.T., Abd Elgawad, A.E.E., 2020. Promoting the decontamination of different types of water pollutants (Cd<sup>2+</sup>, safranin dye, and phosphate) using a novel structure of exfoliated bentonite admixed with cellulose nanofiber. *J. Environ. Manag.* 273, 111130.

Ahmad, S., Ahmad, A., Khan, S., Ahmad, S., Khan, I., Zada, S., Fu, P., 2019. Algal extracts based biogenic synthesis of reduced graphene oxides (rGO) with enhanced heavy metals adsorption capability. *J. Ind. Eng. Chem.* 72, 117–124.

Al-Salem, S.M., Evangelisti, S., Lettieri, P., 2014. Life cycle assessment of alternative technologies for municipal solid waste and plastic solid waste management in the Greater London area. *Chem. Eng. J.* 244, 391–402.

Ali, A., Mahar, R.B., Soomro, R.A., Sherazi, S.T.H., 2017. Fe<sub>3</sub>O<sub>4</sub> nanoparticles facilitated anaerobic digestion of organic fraction of municipal solid waste for enhancement of methane production. *Energy Sources, Part A Recovery, Util. Environ. Eff.* 39 (16), 1815–1822.

Anthony, R., Sims, R., 2013. Cationic starch for microalgae and total phosphorus removal from wastewater. *J. Appl. Polym. Sci.* 130 (4), 2572–2578.

APHA, 2005. Standard methods for the examination of water and wastewater, 21st. American Public Health Association (APHA), American Water Works Association (AWWA), and Water Environment Federation (WEF), Washington DC, USA.

Arya, V., Philip, L., 2016. Adsorption of pharmaceuticals in water using Fe<sub>3</sub>O<sub>4</sub> coated polymer clay composite. *Microporous Mesoporous Mater.* 232, 273–280.

Battas, A., Gaidoumi, A.E., Ksakas, A., Kherbeche, A., 2019. Adsorption study for the removal of nitrate from water using local clay. *Sci. World J.* 2019, 9529618.

Begum, S., Aswal, V., Ramasamy, R., 2016. Structural modification in the formation of starch – silver nanocomposites. In: Paper Presented at the Solid State Physics Symposium USA.

Bell, G., Balasundaram, G., Attia, A.B.E., Mandino, F., Olivo, M., Parkin, I.P., 2019. Functionalised iron oxide nanoparticles for multimodal optoacoustic and magnetic resonance imaging. *J. Mater. Chem. B* 7 (13), 2212–2219.

Bhatia, M., Rajulapati, S.B., Sonawane, S., Girdhar, A., 2017. Synthesis and implication of novel poly(acrylic acid)/nanosorbent embedded hydrogel composite for lead ion removal. *Sci. Rep.* 7 (1).

Boki, K., Tanada, S., Miyoshi, T., Yamasaki, R., Ohtani, N., Tamura, T., 1987. Phosphate removal by adsorption to activated carbon. *Jpn. J. Hyg.* 42 (3), 710–720.

Cheviron, P., Gouanvé, F., Espuche, E., 2015. Starch/silver nanocomposite: effect of thermal treatment temperature on the morphology, oxygen and water transport properties. *Carbohydr. Polym.* 134, 635–645.

Crini, G., 2003. Studies on adsorption of dyes on beta-cyclodextrin polymer. *Bioresour. Technol.* 90 (2), 193–198.

Crini, G., 2006. Non-conventional low-cost adsorbents for dye removal: a review. *Bioresour. Technol.* 97 (9), 1061–1085.

Dai, J., Yang, H., Yan, H., Shangguan, Y., Zheng, Q., Cheng, R., 2011. Phosphate adsorption from aqueous solutions by disused adsorbents: chitosan hydrogel beads after the removal of copper(II). *Chem. Eng. J.* 166 (3), 970–977.

De Castro, L., Brandão, V., Bertolino, L., De Souza, W., Teixeira, V., 2019. Phosphate adsorption by montmorillonites modified with Lanthanum/iron and a laboratory test using water from the Jacarepaguá Lagoon (RJ, Brazil). *J. Braz. Chem. Soc.*

Delval, F., Crini, G., Vebrel, J., Knorr, M., Sauvign, G., Conte, E., 2003. Starch-modified filters used for the removal of dyes from waste water. *Macromol. Symp.* 203 (1), 165–172.

Eng, C.C., Ibrahim, N.A., Zainuddin, N., Ariffin, H., Yunus, W.M.Z.W., Then, Y.Y., Teh, C.C., 2013. Enhancement of mechanical and thermal properties of poly(lactic acid)/polycaprolactone blends by hydrophilic nanoclay. *Indian J. Mater. Sci.* 2013, 1–11.

Fan, C., Zhang, Y., 2018. Adsorption isotherms, kinetics and thermodynamics of nitrate and phosphate in binary systems on a novel adsorbent derived from corn stalks. *J. Geochem. Explor. Indian J. Mater. Sci.* 188, 95–100.

Gratuito, M.K.B., Panyathanmaporn, T., Chumnanklang, R.A., Sirinuntawittaya, N., Dutta, A., 2008. Production of activated carbon from coconut shell: optimization using response surface methodology. *Bioresour. Technol.* 99 (11), 4887–4895.

Guibal, E., 2004. Interactions of metal ions with chitosan-based sorbents: a review. *Separ. Purif. Technol.* 38 (1), 43–74.

Ho, Y.-S., Chiu, W.-T., Wang, C.-C., 2005. Regression analysis for the sorption isotherms of basic dyes on sugarcane dust. *Bioresour. Technol.* 96 (11), 1285–1291.

Ho, Y.S., McKay, G., 1999. Pseudo-second order model for sorption processes. *Process Biochem.* 34 (5), 451–465.

Huang, W., Zhang, Y., Li, D., 2017. Adsorptive removal of phosphate from water using mesoporous materials: a review. *J. Environ. Manag.* 193, 470–482.

Hussain, S., Aziz, H.A., Isa, M.H., Ahmad, A., Van Leeuwen, J., Zou, L., Beecham, S., Umar, M., 2011. Orthophosphate removal from domestic wastewater using limestone and granular activated carbon. *Desalination* 271 (1), 265–272.

Jiang, H., Chen, P., Luo, S., Tu, X., Cao, Q., Shu, M., 2013. Synthesis of novel nanocomposite Fe<sub>3</sub>O<sub>4</sub>/ZrO<sub>2</sub>/chitosan and its application for removal of nitrate and phosphate. *Appl. Surf. Sci.* 284, 942–949.

Juang, R.-S., Yei, Y.-C., Liao, C.-S., Lin, K.-S., Lu, H.-C., Wang, S.-F., Sun, A.-C., 2018. Synthesis of magnetic Fe<sub>3</sub>O<sub>4</sub>/activated carbon nanocomposites with high surface area as recoverable adsorbents. *J. Taiwan Inst. Chem. Eng.* 90, 51–60.

Kavitha, A., 2017. Synthesis and Characterization of Iron Oxide-Chitosan Nano Composite.

Kilpimaa, S., Runtti, H., Kangas, T., Lassi, U., Kuokkanen, T., 2015. Physical activation of carbon residue from biomass gasification: novel sorbent for the removal of phosphates and nitrates from aqueous solution. *J. Ind. Eng. Chem.* 21, 1354–1364.

Krystijan, M., Khachatryan, G., Grabacka, M., Krzan, M., Witczak, M., Grzyb, J., Woszczak, L., 2021. Physicochemical, bacteriostatic, and biological properties of starch/chitosan polymer composites modified by graphene oxide, designed as new bionanomaterials. *Polymers* 13 (14), 2327.

Kumar, M., Chen, H., Sarsaiya, S., Qin, S., Liu, H., Awasthi, M.K., Kumar, S., Singh, L., Zhang, Z., Bolan, N.S., Pandey, A., Varjani, S., Taherzadeh, M.J., 2021. Current research trends on micro- and nano-plastics as an emerging threat to global environment: a review. *J. Hazard Mater.* 409, 124967.

Kumar, M., Rathour, R., Singh, R., Sun, Y., Pandey, A., Gnansounou, E., Andrew Lin, K.-Y., Tsang, D.C.W., Thakur, I.S., 2020. Bacterial polyhydroxyalkanoates: opportunities, challenges, and prospects. *J. Clean. Prod.* 263, 121500.

- Kurtan, U., Amir, M., Baykal, A., 2015. A  $\text{Fe}_3\text{O}_4@\text{Nico}@\text{Ag}$  nanocatalyst for the hydrogenation of nitroaromatics. *Chin. J. Catal.* **36** (5), 705–711.
- Langmuir, I., 1917. The constitution and fundamental properties of solids and liquids. II. Part I. Solids. *J. Am. Chem. Soc.* **39** (9), 1848–1906.
- Li, Y., Jin, H., Liu, W., Su, H., Lu, Y., Li, J., 2018. Study on regeneration of waste powder activated carbon through pyrolysis and its adsorption capacity of phosphorus. *Sci. Rep.* **8** (1).
- Liu, J., Dai, C., Hu, Y., 2018. Aqueous aggregation behavior of citric acid coated magnetite nanoparticles: effects of pH, cations, anions, and humic acid. *Environ. Res.* **161**, 49–60.
- Liu, Q., Hu, P., Wang, J., Zhang, L., Huang, R., 2016. Phosphate adsorption from aqueous solutions by zirconium (IV) loaded cross-linked chitosan particles. *J. Taiwan Inst. Chem. Eng.* **59**, 311–319.
- Liu, X., Zhang, L., 2015. Removal of phosphate anions using the modified chitosan beads: adsorption kinetic, isotherm and mechanism studies. *Powder Technol.* **277**, 112–119.
- Lu, D.R., Xiao, C.M., Xu, S.J., 2009. Starch-based completely biodegradable polymer materials. *Express Polym. Lett.* **3** (6), 366–375.
- Maity, D., Agrawal, D.C., 2007. Synthesis of iron oxide nanoparticles under oxidizing environment and their stabilization in aqueous and non-aqueous media, **308** (1), 46–55.
- Manocha, S., Patel, N., Manocha, L., 2008. Development and characterisation of nanoclays from Indian clays. *Defence Sci. J.* **58** (4), 517–524.
- Mazhandu, Z.S., Muzenda, E., Mamvura, T.A., Belaid, M., Nhubu, T., 2020. Integrated and consolidated review of plastic waste management and bio-based biodegradable plastics: challenges and opportunities. *Sustainability* **12** (20), 8360.
- Metcalfe, L., Eddy, H.P., 2014. *Wastewater engineering: Treatment and Resource Recovery*, fifth ed. McGraw-Hill Education (Metcalfe & Eddy, Inc., New York, USA).
- Moharir, R.V., Kumar, S., 2019. Challenges associated with plastic waste disposal and allied microbial routes for its effective degradation: a comprehensive review. *J. Clean. Prod.* **208**, 65–76.
- Nagoya, S., Nakamichi, S., Kawase, Y., 2019. Mechanisms of phosphate removal from aqueous solution by zero-valent iron: a novel kinetic model for electrostatic adsorption, surface complexation and precipitation of phosphate under oxic conditions. *Separ. Purif. Technol.* **218**, 120–129.
- Nakarmi, A., Bourdo, S.E., Ruhl, L., Kanel, S., Nadagouda, M., Kumar Alla, P., Pavel, I., Viswanathan, T., 2020. Benign zinc oxide betaine-modified biochar nanocomposites for phosphate removal from aqueous solutions. *J. Environ. Manag.* **272**, 111048.
- Nodeh, R.H., Sereshti, H., Zamiri Afsharian, E., Nouri, N., 2017. Enhanced removal of phosphate and nitrate ions from aqueous media using nanosized lanthanum hydrous doped on magnetic graphene nanocomposite. *J. Environ. Manag.* **197**, 265–274.
- Nordin, N., Othman, S.H., Rashid, S.A., Basha, R.K., 2020. Effects of glycerol and thymol on physical, mechanical, and thermal properties of corn starch films. *Food Hydrocolloids* **106**, 105884.
- Padmavathy, K.S., Madhu, G., Haseena, P.V., 2016. A study on effects of pH, adsorbent dosage, time, initial concentration and adsorption isotherm study for the removal of Hexavalent Chromium (Cr (VI)) from wastewater by magnetite nanoparticles. *Proc. Technol.* **24**, 585–594.
- Pan, G., Li, L., Zhao, D., Chen, H., 2010. Immobilization of non-point phosphorus using stabilized magnetite nanoparticles with enhanced transportability and reactivity in soils. *Environ. Pollut.* **158** (1), 35–40.
- Peleka, E.N., Deliyanni, E.A., 2009. Adsorptive removal of phosphates from aqueous solutions. *Desalination* **245** (1-3), 357–371.
- Reddy, M.M., Vivekanandhan, S., Misra, M., Bhatia, S.K., Mohanty, A.K., 2013. Biobased plastics and bionanocomposites: current status and future opportunities. *Prog. Polym. Sci.* **38** (10), 1653–1689.
- Ren, J., Li, N., Wei, H., Li, A., Yang, H., 2020. Efficient removal of phosphorus from turbid water using chemical sedimentation by  $\text{FeCl}_3$  in conjunction with a starch-based flocculant. *Water Res.* **170**, 115361.
- Saifuddin, M., Kim, S., Aziz, A., Kim, K.S., 2019. Mechanistic study of phosphorus adsorption onto Iron Z-A: spectroscopic and experimental approach. *Appl. Sci.* **9** (22), 4897.
- Sandhya, J., Kalaiselvam, S., 2020. Biogenic synthesis of magnetic iron oxide nanoparticles using inedible borassus flabellifer seed coat: characterization, antimicrobial, antioxidant activity and in vitro cytotoxicity analysis. *Mater. Res. Express* **7** (1), 015045.
- Santos, A.F., Arim, A.L., Lopes, D.V., Gando-Ferreira, L.M., Quina, M.J., 2019. Recovery of phosphate from aqueous solutions using calcined eggshell as an eco-friendly adsorbent. *J. Environ. Manag.* **238**, 451–459.
- Sarkar, A., Biswas, S.K., Pramanik, P., 2010. Design of a new nanostructure comprising mesoporous  $\text{ZrO}_2$  shell and magnetite core ( $\text{Fe}_3\text{O}_4@m\text{ZrO}_2$ ) and study of its phosphate ion separation efficiency. *J. Mater. Chem.* **20** (21), 4417–4424.
- Shirsath, S.R., Hage, A.P., Zhou, M., Sonawane, S.H., Ashokkumar, M., 2011. Ultrasound assisted preparation of nanoclay bentonite-FeCo nanocomposite hybrid hydrogel: a potential responsive sorbent for removal of organic pollutant from water. *Desalination* **281**, 429–437.
- Syafiq, R., Sapuan, S.M., Zuhri, M.R.M., 2021. Antimicrobial activity, physical, mechanical and barrier properties of sugar palm based nanocellulose/starch biocomposite films incorporated with cinnamon essential oil. *J. Mater. Res. Technol.* **11**, 144–157.
- Tan, W.-f., Lu, S.-j., Liu, F., Feng, X.-h., He, J.-z., Koopal, L.K., 2008. Determination of the point-of-zero charge of manganese oxides with different methods including an improved salt titration method. *Soil Sci.* **173** (4), 277–286.
- Tarique, J., Sapuan, S.M., Khalina, A., 2021. Effect of glycerol plasticizer loading on the physical, mechanical, thermal, and barrier properties of arrowroot (*Maranta arundinacea*) starch biopolymers. *Sci. Rep.* **11** (1).
- Tay, T., Ucar, S., Karagöz, S., 2009. Preparation and characterization of activated carbon from waste biomass. *J. Hazard Mater.* **165** (1-3), 481–485.
- UNDP, 2021. Retrieved from <https://feature.undp.org/plastic-tidal-wave/#article>.
- Vasudevan, R., Ramalinga Chandra Sekar, A., Sundarakannan, B., Velkennedy, R., 2012. A technique to dispose waste plastics in an ecofriendly way – application in construction of flexible pavements. *Construct. Build. Mater.* **28** (1), 311–320.
- Waweru, N.M., Yang, J., Bolokonya, H.C., 2019. Enhanced removal of phosphates by the adsorbent consisting of iron oxide loaded on porous chitosan/cellulose acetate particle. *Engineering* **11** (7), 366–394.
- Weber, W.J., Morris, J.C., 1963. Kinetics of adsorption on carbon from solution. *J. Sanit. Eng. Div.* **89** (2), 31–60.
- Xie, J., Wang, Z., Lu, S., Wu, D., Zhang, Z., Kong, H., 2014. Removal and recovery of phosphate from water by lanthanum hydroxide materials. *Chem. Eng. J.* **254**, 163–170.
- Yang, F., Zhang, S., Sun, Y., Tsang, D.C.W., Cheng, K., Ok, Y.S., 2019. Assembling biochar with various layered double hydroxides for enhancement of phosphorus recovery. *J. Hazard Mater.* **365**, 665–673.
- Yoon, S.Y., Lee, C.G., Park, J.A., Kim, J.H., Kim, S.B., Lee, S.H., Choi, J.W., 2014. Kinetic, equilibrium and thermodynamic studies for phosphate adsorption to magnetic iron oxide nanoparticles. *Chem. Eng. J.* **236**, 341–347.
- Zhang, Y., Mazumder, A., Zhang, T.C., Dai, C., 2015. The application of advanced materials on the water or wastewater treatment. *J. Chem.* **2015**, 1–2.
- Zheng, Y., Yanful, E.K., Bassi, A.S., 2005. A review of plastic waste biodegradation. *Crit. Rev. Biotechnol.* **25** (4), 243–250.